

## O<sub>3</sub> and NO<sub>2</sub> vertical columns using SAOZ UV-Visible spectrometer

A. Pazmiño<sup>a</sup>

LATMOS, CNRS and University of Versailles Saint Quentin, Guyancourt, France

**Abstract.** This chapter presents an overview of ground-based SAOZ spectrometer for measurements of O<sub>3</sub> and NO<sub>2</sub> total vertical columns. Due to instrument conception (zenith measurement in the Visible), the SAOZ is the only instrument that could measure continuously and at all latitudes up to the polar circle in winter. It can be operated in bad weather conditions (cloudy, rainy or snowing) and it has the advantage of spectral self-calibration and completely automatic mode. Differential Optical Absorption Spectroscopy technique is used allowing a self-calibration of different atmospheric constituents on the respective absorption cross-section.

### 1 Introduction

The SAOZ (Système d'Analyse par Observation Zénithale [1]) instrument is part of the Network for the Detection of Atmospheric Composition Change (NDACC) international network. There are 17 SAOZ owned by CNRS and other institutes at all latitudes including in the tropics. The SAOZ has been developed at Service d'Aéronomie (now LATMOS) in the late 1980s following the discovery of the ozone hole in Antarctica. The first SAOZ has been installed in 1988 at Dumont d'Urville in Antarctica to measure stratospheric ozone at high latitudes during the polar winter. The conventional techniques for measuring ozone in the ultraviolet range are useless for solar zenith angles with the sun low on the horizon. In contrast, the SAOZ, which measures in the visible, allows the continuous monitoring of ozone up to 91° Solar Zenith Angle (SZA) that is throughout the winter at the polar circle. In addition to the daily integrated ozone column, the SAOZ measures also total NO<sub>2</sub> and detects the presence of polar stratospheric clouds from a color index or CI [2, 3].

This chapter is arranged as follows: introduction is succeeded by a description of the instrument. DOAS technique used for ozone and NO<sub>2</sub> SAOZ retrieval is explained in section 3. Then, different studies using SAOZ ozone measurements are presented in section 4 and finally the conclusions.

### 2 SAOZ spectrometer

The SAOZ is a passive remote-sensing instrument that measures the sunlight scattered from the zenith sky. It was designed to allow observations of O<sub>3</sub> and NO<sub>2</sub> total vertical column amounts. For geometrical reasons, most precise measurements are performed twice a day during twilight (sunrise and sunset). The SAOZ can be divided in three parts (see Fig. 1): the "SAOZ Unit" where spectrometer and electronics are located, the "Interface Box" to link the SAOZ Unit to the last part of the instrument, the "Retrieval Device".

---

<sup>a</sup> e-mail: andrea.pazmino@latmos.ipsl.fr

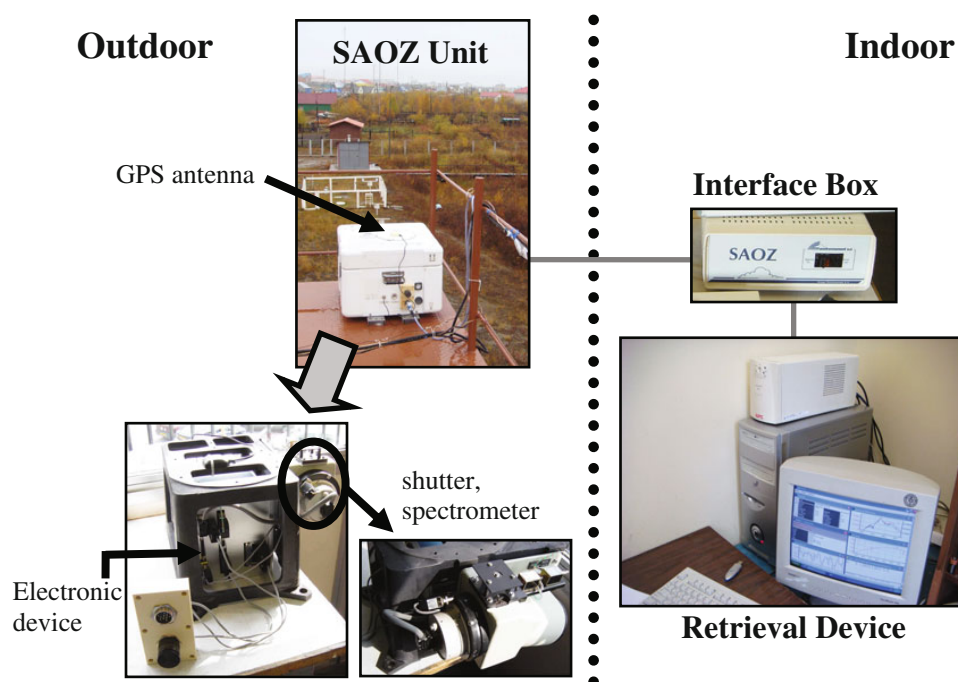


Fig. 1. Configuration of SAOZ instrument.

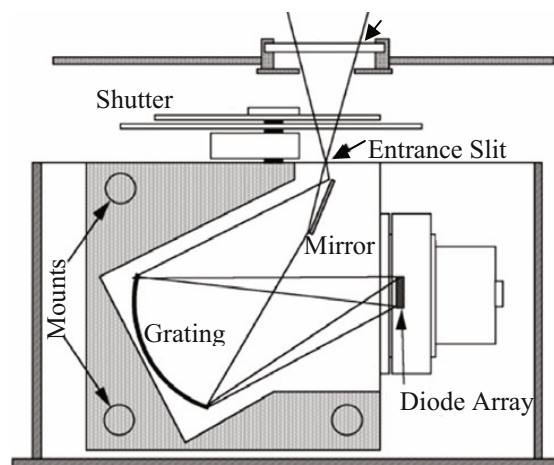


Fig. 2. Optical scheme of SAOZ instrument.

The SAOZ Unit is placed outdoor in a sealed tight and dehydrated box on the top of which a quartz window is mounted in order to look at the zenith sky with a half field of view of  $10^\circ$ . A quartz material is used to allow detection of ultraviolet and visible light. Inside the box, the spectrometer and driving devices are installed. Figure 2 shows the optical scheme of the instrument. The entrance slit and the grating are adapted to allow an average resolution of the order of 1 nm in the range 300–600 nm. The field of view is limited by baffles between the quartz window and a shutter in order to take into account the aperture of the spectrometer. The spectrometer is made of a commercial flat field broad-band Jobin-Yvon CP200 equipped with a holographic grating and a Hamamatsu uncooled diode array. The focal length of grating is  $F = 190$  mm and the aperture is  $F/3$ .

The first version (SAOZ-512) was using a 200 gr/mm grating and  $25\mu$  entrance slit adapted to a 512 diode array detector (pixel size of  $25\mu$ ) and the second one (SAOZ-1024) was using a 360 gr/mm grating and  $50\mu$  entrance slit associated to a 1024 diode array detector (pixel size of  $25\mu$ ) allowing a better oversampling (2 instead of 1). As SAOZ was designed to measure especially in the Polar Regions, sometimes of difficult access, the system is completely automated; no maintenance except for the only moving part (mechanical shutter). The shutter allows measurements of dark current. The shutter could be a rotating disc or a push-pull controlled by the electronic device. The most recent SAOZ use the latter kind of shutter for cost reasons.

The electronic device consists of five electronic boards. One of the boards is used for acquisition of the spectrum or dark current coming from the pre-amplifier device placed after the detector. Another electronic board is used to drive the shutter and monitor the temperature of the box and detector. The third board provides different power supply values required to operate. Another board is the CPU where different programs are installed for acquisition and tests. The last board corresponds to the electronics of GPS. The GPS's antenna is placed outside the box device.

The Interface Unit allows three kind of communication between the SAOZ Unit and the external computer: operational mode (Real Time), Monitor mode to communicate with the CPU inside the SAOZ Unit to change the configuration of the instrument and finally a parallel connection to change the onboard software.

According to the software stored on the CPU board, the measurements are performed from sunrise to sunset until a SZA of  $96^\circ$ . The exposure time is adjusted automatically between 0.1 s to 60 s in order to optimize the signal and the spectra are co-added in memory during a 60 s duty cycle. The dark current of the detector is measured each time the duration of exposure changes and subtracted. The sampling time of the measurement, SZA as a function of latitude and longitude of the station already stored are computed for the acquisition using time given by GPS. The configuration of the instrument is stored in the CPU and there is also the possibility to store the spectra.

The instrument is driven by an external computer which records and analyses the spectra in real time (figure 1). Spectra and analysed ozone and  $\text{NO}_2$  slant columns are stored locally on the "Retrieval Device" and transmitted everyday to the laboratory through internet. Vertical columns of  $\text{O}_3$  and  $\text{NO}_2$  are calculated at laboratory from the weighted average of  $\text{O}_3$  and  $\text{NO}_2$  slant columns measured between  $86^\circ$  and  $91^\circ$  SZA using modelled Air Mass Factor (AMF). Real time data are available in SAOZ web page (<http://saoz.obs.uvsq.fr/>) and reprocessed data with the up to date settings are transmitted regularly, once a year, to NDACC after reception of original spectra at the laboratory from the remote stations.

### 3 SAOZ spectral analyses

The retrieval method used by SAOZ referred to as Differential Optical Absorption Spectroscopy (DOAS, [4]). This technique is suitable for the detection of minor gases in the atmosphere. In the case of zenith-sky viewing, twilight geometry (SZA near  $90^\circ$ ) allows long light path into the stratosphere ( $\sim 200$  km) and thus a high sensitivity to detect stratospheric minor constituents like ozone and  $\text{NO}_2$ . Figure 3 shows the geometry of observation of SAOZ measurements for different SZA.

Case (1) corresponds to SZA much lower than  $90^\circ$  when light rays cross obliquely the atmosphere. The measurements are sensitive to both stratospheric and tropospheric molecules. On the other hand, case (2) represents twilight geometry (SZA near  $90^\circ$ ) when light rays go horizontally through the stratosphere and cross vertically the lower atmosphere. In that configuration stratospheric measurements ( $86^\circ$  to  $91^\circ$  SZA) are not perturbed by tropospheric contribution.

The SAOZ data are arranged in three levels:

- a) Level 0 corresponds to the spectrum where dark current is already removed. Ancillary data are also included such as time, SZA, GPS location, exposure time, summation, and temperature inside the instrument.
- b) Level 1 is the slant column (number of molecules along line-of-sight) of ozone and  $\text{NO}_2$  after application of DOAS technique. The method correlates differential narrow features of different

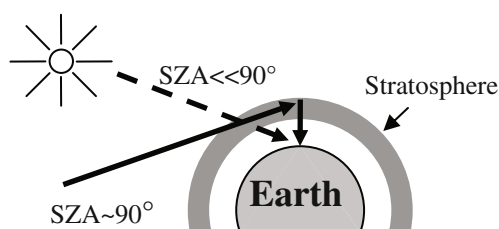


**Fig. 3.** Path length of solar radiation crossing the atmosphere up to SAOZ instrument for SZA much lower and near 90°.

atmospheric species after removal of broadband signal due to Raman and Rayleigh scattering, with the corresponding differential absorption cross-section of the constituents.

- c) Level 2 is associated to the vertical columns of O<sub>3</sub> and NO<sub>2</sub> resulting from the conversion of slant columns using the so-called air mass factors (AMFs).

### 3.1 Slant column retrieval

The attenuation of solar radiation travelling through the atmosphere is explained by the Beer-Lambert law usually written:

$$I = I_0 e^{-\tau} \quad (1)$$

where  $I_0$  and  $I$  are radiation before and after crossing the atmosphere respectively and  $\tau$  is the optical thickness of the atmosphere represented as follows:

$$\tau = \sum \sigma_i(\lambda) * NL_i + \varepsilon_R(\lambda) + \varepsilon_M(\lambda) \quad (2)$$

where the first right term correspond to absorption ( $\sigma$  the absorption cross-section of different constituents and  $NL$  the slant column) and the second and third terms the Rayleigh and Mie scattering, respectively.

The optical absorption spectroscopy equation can be written as follows:

$$\tau = \ln \frac{I_0(\lambda)}{I(\lambda)} = \sum \sigma_i(\lambda) * NL_i + \varepsilon(\lambda). \quad (3)$$

In the case of SAOZ measurements, the optical thickness is equal to the logarithm of the ratio between each measured spectrum ( $I$ ) and the reference spectrum ( $I_0$ ). The reference spectrum is generally recorded at low SZA (~45°) on a clear and unpolluted day to reduce the contribution of the absorption by molecules along the optical path. It is measured by the same instrument and at the same location.

In order to ensure a self-calibration on wavelength at each measurement, 15 Fraunhofer solar absorption lines are used for precise wavelength alignment of the signal on the reference spectrum. These lines are used since they are very deep and easily recognized. A parabolic fitting is used to shift and stretch the measured spectrum by least-square correlation between measured and reference spectra. Figure 4 shows the signal and reference spectra and the 15 Fraunhofer lines used for wavelength fitting. The correspondence detector pixel/wavelength is determined by looking at the exact Fraunhofer lines position in an atlas of high resolution (0.005 nm) solar lines [5]. The wavelength law and the instrument resolution are done by degrading the high resolution solar spectrum to match the reference spectrum resolution.

Then, the DOAS technique expressed in equation 4 is applied. This technique removes the monotonic large trends (2<sup>nd</sup> and 3<sup>rd</sup> right terms on Eq. (2)) and represented in equation 3 by  $\varepsilon$ . This is done by subtracting the same spectrum smoothed at a broad bandpass (40 nm) resulting in an atmospheric differential spectrum, into which narrow features corresponding to absorption by O<sub>3</sub>, NO<sub>2</sub>, O<sub>4</sub> (oxygen dimer), H<sub>2</sub>O, O<sub>2</sub> and OCIO, are remaining.

$$\Delta\tau = \sum \Delta\sigma_i(\lambda) * NL_i. \quad (4)$$

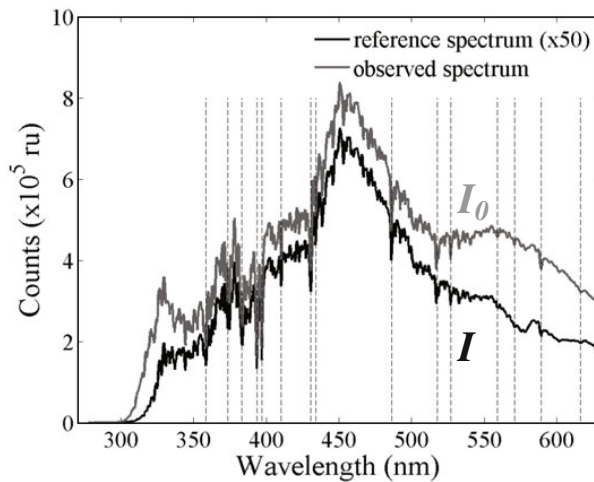


**Fig. 4.** Spectrum measured at SZA = 90° on August 25, 2010 at ScoresbySund station (70.5°N, 22°W) and reference spectrum obtained at high sun position (SZA = 50°) of summer 2002. Fraunhofer absorption lines are represented by dash lines.

Finally, slant column of each constituent ( $NL_i$  in Eq. (4)) is calculated by least squares fitting between the differential signal  $\Delta\tau_i$  and the differential laboratory cross-sections  $\Delta\sigma_i$  of each absorber in an iterative process in which the contributions of the various species are calculated and removed sequentially using filters. The width of such filters and the spectral analysis window are adapted to the characteristics of each absorber to reduce interference and enhance absorber features. Furthermore, the analysis is performed iteratively to minimize interference between constituents. For example ozone presents structures of 10 nm width in the visible between 450 and 550 nm and a low pass filter is applied to remove signatures of higher frequency as  $\text{NO}_2$  ones, which presents narrower features of 1 nm. In the first iteration, ozone is calculated in a small spectral window where  $\text{NO}_2$  is poorly absorbing. Then after having removed  $\text{NO}_2$  in the iteration,  $\text{O}_3$  can be retrieved in a larger spectral window. The differential method allows a self-calibration of constituents on the respectively absorption cross-sections.

Ring effect linked to wavelength redistribution of photons due to Raman scattering [6] has to be considered in the iterations steps since it perturbs all constituents in the whole spectral range. A high resolution Ring effect signature or “cross-section” is generated following Chance and Spurr [7] method. This “cross-section” is convolved to the instrumental resolution. Ring effect is particularly highlighted around Fraunhofer lines where the lines are deformed (less intense and wider). Then, differential “cross-section” of Ring effect is correlated with the differential optical thickness in 405–445 nm spectral range where 410.3 nm, 430.7 nm and 434.2 nm Fraunhofer lines are present (see Fig. 4). Others spectral ranges with pronounced lines are also considered: 466–495 nm and 515–537 nm.

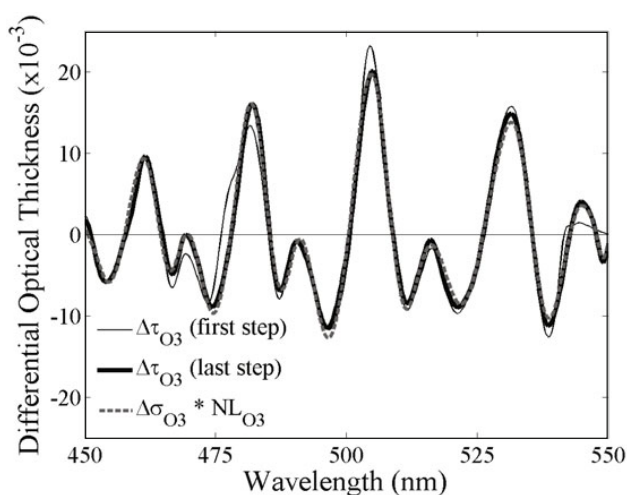
High resolution differential absorption cross-sections aligned with the wavelength law and convolved with the instrument slit function are used. Ozone is measured in the Chappuis visible bands (450–550 nm) where the cross sections are weakly dependant of the temperature;  $\text{NO}_2$  in 410–530 nm range;  $\text{O}_4$  in 440–544 nm;  $\text{H}_2\text{O}$  in one band 500–555 nm and  $\text{O}_2$  around 620 nm. Cross-sections settings recommended by NDACC UV-Vis Working Group, especially for ozone retrieval are shown in Table 1 (adapted from [8]).

Figure 5 shows differential optical thickness of ozone resulting from the first and last iteration steps of spectral analysis. This figure highlights the improvement between step 1 (thin line) and step 5 (thick line), since features of  $\Delta\tau_i$  in the last step present better correlation with the ones of  $\Delta\sigma_i$  represented by the grey dash line.

The slope coefficient of the correlation between differential optical thickness and differential absorption cross-section of Fig. 5 gives the slant column amount of ozone  $NL_{\text{O}_3}$  and the standard deviation of the correlation represents the  $1\sigma$  incertitude on the measurement.

**Table 1.** Settings recommended for the UV-visible retrieval of O<sub>3</sub> vertical columns (adapted from [8]).

Parameter	Recommendation
Fitting interval for O <sub>3</sub>	450–550 nm
Wavelength calibration	based on reference spectrum
Cross sections	
O <sub>3</sub>	[9], 223 °K
NO <sub>2</sub>	[10], 220 °K
H <sub>2</sub> O	[11], Hitran 2004
O <sub>4</sub>	Hermans ( <a href="http://spectrolab.aeronomie.be/o2.htm">http://spectrolab.aeronomie.be/o2.htm</a> )
Ring effect	NDACC source for Ring effect correction
AMF calculation for O <sub>3</sub>	BIRA-IASB O <sub>3</sub> AMF LUTs
Residual amount in reference spectrum	Monthly Langley plot [12]
SZA range	86°–91° SZA

**Fig. 5.** Ozone spectral analysis: differential optical thickness of ozone for the first (thin line) and fifth (thick line) iteration. Differential ozone absorption cross section multiplied by slant column is represented by grey dash line.

Slant column of each constituent  $NL_i$  is expressed as follows:

$$NL_i = \frac{\Delta\tau_i}{\Delta\sigma_i}. \quad (5)$$

Figure 6 displays  $\Delta\tau_i$  and  $\Delta\sigma_i$  multiplied by  $NL_i$  where  $i$  is equal to NO<sub>2</sub>, O<sub>4</sub> and H<sub>2</sub>O after last step of spectral analysis (top panels). Differential optical thickness of each constituent presents good correlation with the corresponding differential absorption cross-section and after five iterations interferences of others known absorbers in the spectral range are negligible.

Panel d) of Fig. 6, shows a polynomial fitting used to spectral calibration. This fitting presents a small shifting and stretching of spectrum with a maximum difference between short and long wavelengths lower than 0.2 pixel (0.06 nm) meaning that spectral changes due to instrument temperature are limited and taken into account in the special alignment.

Panels e) and f) of Fig. 6 show the absolute and differential optical thickness obtained before (grey curves) and after (black curves) spectral analysis. Looking at these curves, all signatures have been correctly removed from the signal after analysis. The absolute optical thickness after analysis in panel e) shows only Rayleigh and Mie typical contribution without the different features of ozone and others absorbers. The residual in differential optical thickness after removal of constituent's signatures is lower than 3/1000 as shown by the black curve in panel f) of Fig. 6.

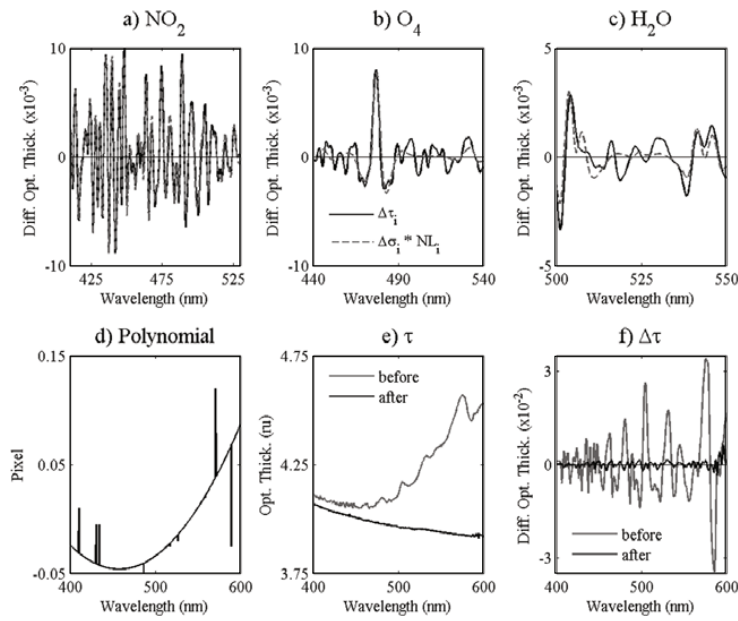


**Fig. 6.** Top panels: Differential optical thickness and differential absorption cross-section multiplied by calculated slant column of a)  $\text{NO}_2$ , b)  $\text{O}_4$  and c)  $\text{H}_2\text{O}$  after spectral analysis. Bottom panels: d) polynomial curve used for wavelength fitting, e) signal before and after correction of all identified constituents and f) differential optical thickness before and after spectral analysis.

### 3.2 Vertical column retrieval

The conversion of slant columns relative to a given reference spectrum into vertical columns requires the knowledge of the optical path of the light scattered at zenith, that is the AMF, and the residual amount of constituent present in the reference spectrum. Equation 6 shows the calculation of vertical column for ozone ( $N_{\text{O}_3}$ ):

$$N_{\text{O}_3} = \frac{NL_{\text{O}_3} + NL_{\text{refO}_3}}{AMF_{\text{O}_3}} \quad (6)$$

where  $NL_{\text{refO}_3}$  is the residual amount of ozone in the reference spectrum and  $AMF_{\text{O}_3}$  the ozone AMF.

#### 3.2.1 AMF

The AMF is calculated by modelling the radiative transfer of the sunlight into the atmosphere. It is dependant of constituent (concentration and altitude of peak), aerosols, density profiles and wavelength. In the visible at 500 nm, the average atmospheric scattering layer at  $90^\circ$  SZA is located around 10–12 km, which is below the ozone and nitrogen dioxide peak concentration and above tropospheric clouds.

In the past, single AMF using yearly mean profiles for Tropics, Mid-latitudes or Polar regions depending on the station for both  $\text{O}_3$  and  $\text{NO}_2$  was used. For example,  $\text{O}_3$  and  $\text{NO}_2$  Polar AMF were calculated from summer evening composite profiles from satellite POAM III/SPOT 4 and SAOZ balloon sonde. The AMF is calculated at the centred wavelength of the fitting band: at 510 nm for  $\text{O}_3$  and 470 nm for  $\text{NO}_2$ . At  $90^\circ$  SZA the Polar AMF were respectively 16.6 for  $\text{O}_3$  and 16.1 for  $\text{NO}_2$ .

Nowadays, a daily AMF for ozone calculated by UVSPEC/DISORT radiative transfer model [13] is implemented in SAOZ V2 retrieval. The model uses a multi-entry data base using TOMS version 8 (TV8) ozone and temperature profile climatology [14]. The TV8 is a monthly-zonal climatology sorted according to the ozone column. The parameters considered are wavelength, ground albedo,

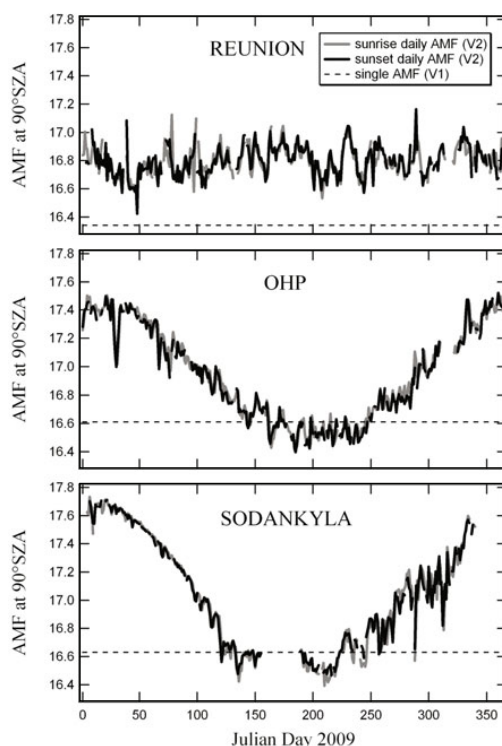


**Fig. 7.** Seasonal variation of daily and single O<sub>3</sub> AMFs at 90° SZA in 2009 at Reunion (21°S, 55°E), Observatoire de Haute Provence (OHP), France (44°S, 6°E) and Sodankyla, Finland (67°N, 27°E). The SAOZ tropical, mid- and high-latitude O<sub>3</sub> AMF values at 90° SZA are 16.3, 16.6 and 16.6, respectively (dash lines).

latitude, altitude, total ozone amount and SZA. The wavelength was fixed at 510 nm, the centred on the fitting band. In order to illustrate the impact of using new daily O<sub>3</sub> AMF (SAOZ V2 algorithm), Figure 7 shows the yearly evolution of daily AMF at 90° SZA and single AMF used in former SAOZ V1 retrieval for tropical mid- and high-latitude stations.

In the case of Sodankyla, Finland and Observatoire de Haute Provence (OHP), France (high and mid-latitudes, respectively), the largest difference was obtained in winter with daily AMFs larger than the SAOZ ones by up to 6%. In summer, the difference is in the 0–1% range, with daily AMFs generally lower than the SAOZ V1. In the tropics (Reunion station), the daily AMFs are systematically larger than the SAOZ AMF V1 by up to 4%, with no seasonal difference.

### 3.2.2 Residual

The residual amount is determined by monthly Bouguer-Langley plot (slant column versus AMF) extrapolated to zero air mass (Vaughan et al., 1997). Another way to show Bouguer-Langley plots is to display vertical column of constituent as a function of AMF. Figure 8 shows Bouguer-Langley plots for January and July 2009 at OHP. The residual O<sub>3</sub> amount of the reference spectrum was considered of  $8 \times 10^{18}$  mol./cm<sup>2</sup>. This value was correctly chosen since the curves of Bouguer-Langley plots are mostly flat in different months as shown in Fig. 8. If the chosen residual value is overestimated (underestimated), the curves will present negative (positive) slopes.

The main change between V1 and V2 is the use of O<sub>3</sub> daily AMF. In order to evaluate the impact of new version on SAOZ performances, the dataset were compared to satellite overpass observations, as well as to ground-based collocated Dobson and Brewer measurements at OHP and Sodankyla, respectively [8]. Figure 10 shows the seasonal variation of the Dobson-SAOZ relative difference at

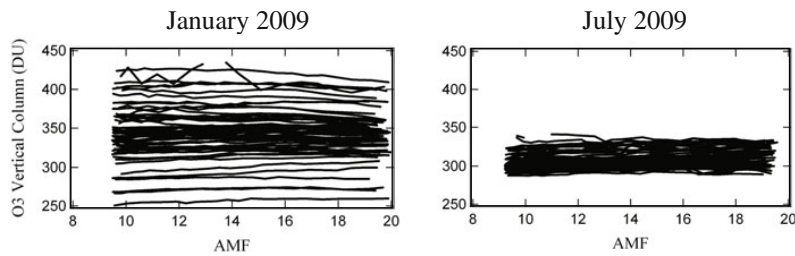


**Fig. 8.** Bouguer-Langley plots corresponding to a residual ozone amount in the slant column of reference spectrum of  $8 \times 10^{18}$  mol./cm<sup>2</sup> (297 DU).

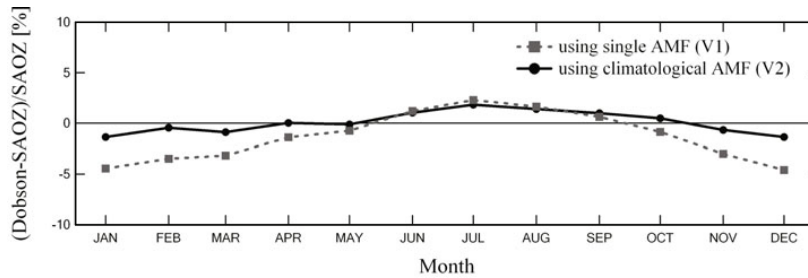


**Fig. 9.** Seasonal variation of the Dobson-SAOZ relative difference at OHP using SAOZ V1 and V2.

OHP considering SAOZ V1 (dashed line) and SAOZ V2 (solid line) to illustrate the advantage using climatological AMF.

The difference shows a systematic seasonal variation with a summer maximum of 1.5%. The improvement between both versions is highlighted by the diminution of the amplitude seasonal variation from 6.9% in V1 to 3.2% in V2. This feature is also observed when comparing with satellites observations and Brewer measurements at Sodankyla, in the Northern Finland.

Finally, the overall error budget on V2 O<sub>3</sub> vertical columns takes into account uncertainties on cross-sections and AMF (vertical profiles of the constituent, stratospheric temperature seasonal changes) and the residual amount in reference spectrum. An error budget of 4.6% is calculated [8].

## 4 Ozone studies

Various scientific activities were achieved using SAOZ measurements in the frame of NDACC. This international network is dedicated to monitor the impact of natural and anthropogenic changes on the stratosphere and the validation of satellite observations. Nowadays, 17 SAOZ located at different latitudes regions are part of NDACC.

SAOZ ozone and NO<sub>2</sub> data are intensively used to evaluate the quality of the measurement of different satellites at all latitudes. SAOZ allows checking of continuity between them and detection possible time-dependent drifts.

The SAOZ instruments located at Polar Regions allow the estimation of the annual amplitude of ozone loss in Arctic and Antarctica. WMO uses this information for its newsletters on the state of the ozone hole and for the Quadrennial Ozone Assessments reports. Studies on Polar Stratospheric Clouds (PSC) were also covered using CI data from Arctic SAOZ instruments.

The long datasets of O<sub>3</sub> and NO<sub>2</sub> (more than 15 years at all latitudes), allow studies of trends taking into account the QBO, the ENSO, solar activity, variations in the intensity of Brewer-Dobson circulation.

In the next sub-sections, the two first ozone studies using SAOZ measurements will be presented.

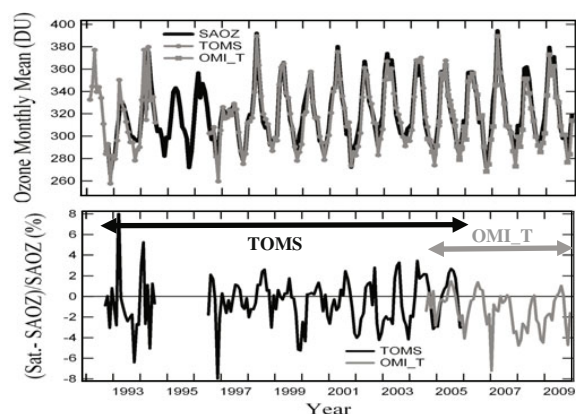


**Fig. 10.** Comparison between SAOZ V2 and satellite (TOMS and OMI-TOMS) overpass total ozone at OHP. Top panel: monthly mean total ozone. Bottom panel: satellite-SAOZ relative difference.

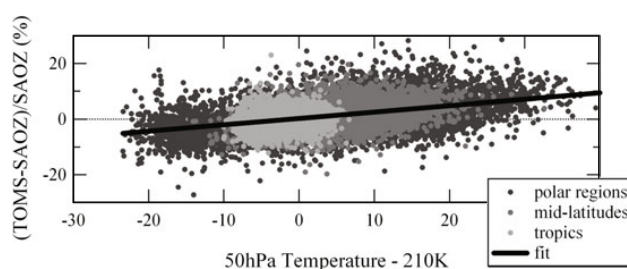


**Fig. 11.** Correlation between daily TOMS-SAOZ difference and ECMWF temperature at 50 hPa for the SAOZ stations in polar, mid-latitude and tropical regions. The correlation fit is shown by the thick line [8].

#### 4.1 Comparison with satellites

Ozone budget in the atmosphere comes from a large number of chemical interactions involving solar radiation and atmospheric minor constituents. Its spatial and temporal distribution on the global scale results from combined effects of photochemistry and transport processes. Only remote sensing observations from a satellite platform can provide spatial ozone measurements. However, satellite instruments are subject to time-dependent drifts. Ozone measurements of satellites working in the ultraviolet are also limited to SZA lower than  $83^\circ$  banishing ozone evaluation studies over regions poleward  $60^\circ$  in winter [15]. High quality ground-based networks such as SAOZ one, are necessary for independent calibration and validation of satellite experiments. Figure 10 displays SAOZ V2 comparison with TOMS V8 series onboard Nimbus-7, Meteor-3 and Earth Probe satellites and OMI-TOMS onboard AURA above OHP station. Ozone monthly mean and monthly mean difference between SAOZ and satellites are shown in top and bottom panels, respectively.

A good agreement is found between SAOZ and satellites, with a mean bias of  $-0.6\%$  for TOMS and  $-1.4\%$  for OMI-TOMS and a seasonal variation of a few percent. GOME, SCIAMACHY and OMI-DOAS spatial observations were also compared showing a mean bias smaller than  $0.5\%$  at OHP with almost no seasonal variation.

Recent paper of Hendrick et al. [8] shows that systematic seasonal variation remaining in the difference satellite-SAOZ V2 is mostly originating from a stratospheric temperature dependence. In order to analyse this, the authors have correlated the daily satellite-SAOZ difference with the corresponding ECMWF temperature at 50 hPa. Since the correlation was performed using data at all latitudes together, the average bias of each station is normalized to zero at 210 K to remove systematic mean differences between the stations. Figure 11 shows the correlation at 50 hPa for TOMS-SAOZ differences at all stations (polar, mid-latitude and tropics).

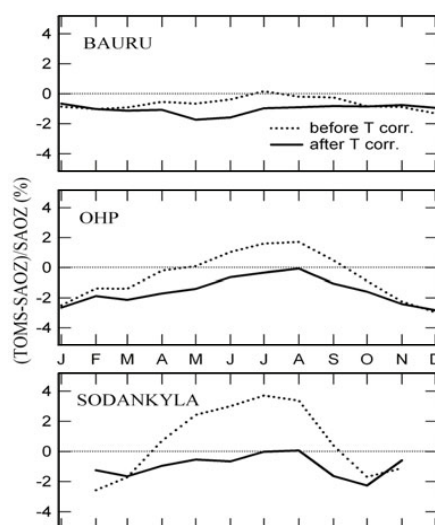


**Fig. 12.** Seasonal variation of the difference between TOMS and SAOZ V2 before (dotted lines) and after (solid lines) temperature correction. From top to bottom: Bauru, Brazil, OHP, France and Sodankyla, Finland.

Since the visible ozone Chappuis bands used by SAOZ are little sensitive to temperature, and satellites measurements are in the spectral UV range, the authors suggest that seasonal variation of the difference between SAOZ and satellites observations in the UV is coming from errors in ozone absorption cross sections in the UV or inadequate correction for temperature dependence in this wavelength region. After correcting for temperature, the amplitude of the seasonal variation of the satellite-SA OZ V2 differences decreases significantly as shown in Fig. 12 for three stations at different latitudes: Bauru at 22°S, 49°W (tropic), OHP (mid-latitude) and Sodankyla (Arctic) [8].

The amplitude of seasonal variation of the difference after temperature correction is highly reduced for the three stations specially highlighted at high latitudes. The amplitude has been decreased 1.5 to 3 times the ones before correction, from 1.5 to 0.7% at Bauru, 4.7 to 2.7% at OHP and 6.3 to 2.3% at Sodankyla. The authors conclude that all UV satellites and ground-based instruments such as the Dobson must be corrected for the temperature dependence in their absorption correction.

#### 4.2 Polar Ozone loss

The processes leading to massive and seasonal ozone destruction in the Polar Regions are relatively well understood. Scientific studies have shown that the formation of the ozone hole requires very low temperatures allowing the formation of polar stratospheric clouds (PSC), an isolated air mass (Polar Vortex), important activated halogenated amounts in the stratosphere and solar radiation. Two-step processes lead to this severe ozone depletion in the stratosphere: 1) a pre-conditioning step in winter, during the polar night where activation of halogenated compounds take place on PSC surface by heterogeneous chemistry processes; and 2) the step concerning the destruction of ozone, which takes place when sunlight is again present in the polar stratosphere and halogen species are able to destroy ozone during catalytic cycles.

It is now important to properly quantify the destruction of one year to another in order to detect the effect of the reduction of halogenated compounds in the stratosphere. The effect of high content of these constituents in the polar stratosphere is different in the Arctic and Antarctic due to weather differences in these two regions in winter. During the Antarctic winter, the stratosphere is characterized by very cold and stable meteorological conditions. The high activation of chlorine compounds resulting in a dramatic increase in the mixing ratio of highly reactive chlorine compounds (Cl, ClO, Cl<sub>2</sub>O<sub>2</sub>) induced by very low temperatures in the polar vortex led to a complete ozone destruction in the lower stratosphere at the end of September. The chemical loss of ozone in Antarctica can be considered

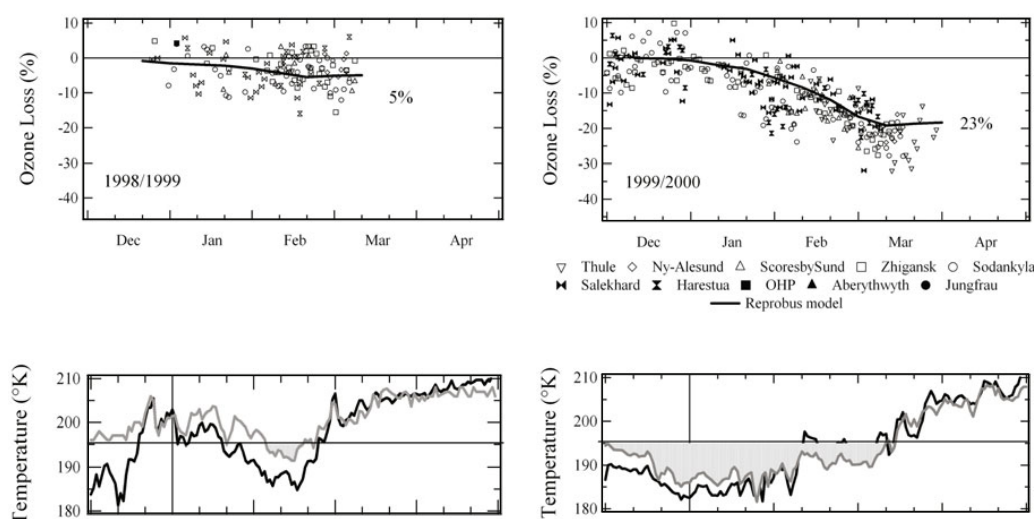


**Fig. 13.** Top panels: Estimated Arctic ozone loss using SAOZ measurements for two years. Bottom panels: temperatures at 475 K (grey curve) and 550 K (black curve) isentropic levels. Horizontal line represents the temperature of PSC formation at 475 K isentropic level (194 °K).

saturated. This saturation should result in a delay in the detection of ozone recovery. In Arctic, because of the conditions of higher temperatures in winter (+10 °C compared to Antarctica), the chemical ozone loss is not saturated and much more variable from year to year, making difficult to detect the signal related to the reduction of halogenated compounds. Climate models can not currently simulate the region in which the polar ozone recovery will be detected first. It is therefore necessary to conduct regular monitoring of ozone loss in both Polar Regions.

SAOZ measurements at Polar Regions are used each year to estimate ozone loss using ozone passive method [16]. The ozone loss is calculated subtracting the measured total ozone inside the polar vortex from the corresponding passive ozone tracer (ozone simulated without interactive chemistry) from chemical transport model (CTM). The position of the station inside or outside the polar vortex is determined using Potential Vorticity (PV) from ECMWF analysis. Figure 13 displays daily difference between total ozone passive tracer of REPROBUS model [17] and SAOZ measurements at each station when located inside the vortex (top panels). Temperature at 475 and 550 K isentropic levels are also shown (bottom panels).

Two years are shown, 1998/1999 winter (left panel) representative of years with weak accumulated ozone loss (5%) and 1999/2000 winter (right panel) where the ozone loss exceeds 20%. This can be explained by the evolution of temperatures at 475 and 550 K isentropic levels displayed in bottom panels of Fig. 13 are very different between these two years. The 1998/1999 winter was very warm. The temperature at both isentropic levels does not reach PSC temperature formation except around February and increases very fast at the end of this month. In contrast, 1999/2000 winter presents low temperatures, already lower than PSC formation one in December and the low temperatures persist at both isentropic levels up to the first week of March. This led to a very different ozone loss for both winters.

Figure 14 shows cumulative ozone loss estimated for both Polar Regions since 1993/1994 winter for Arctic and 1989 winter for Antarctica. The ozone loss is extremely linked to history of stratospheric temperature. Lower temperatures than PSC formation appears each year above Antarctica and persists for long time. In the case of Arctic, the stratospheric temperatures are generally at the limit of PSC formation and cold or warm winters can be observed yielding to relatively high or low ozone loss, respectively. This is the reason of high Arctic ozone loss variability from year to year. The ozone loss in Antarctica has been almost stable these last years with a cumulated ozone loss of 50–60% corresponding to 225–250 DU [18]. In the case of Arctic, cumulated ozone loss of 5–13% (25–60 DU) for warm winters and 20–30% (90–140 DU) for cold ones has been estimated.

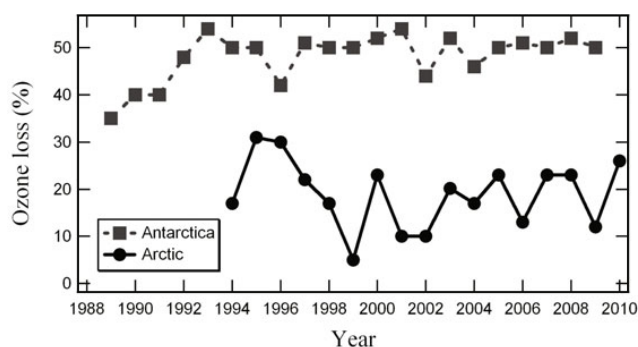


**Fig. 14.** Inter-annual variability of cumulative Arctic and Antarctic ozone loss at the end of each winter since 1993/94 and 1989, respectively (Courtesy of Florence Goutail and Jayan Kuttippurath).

## 5 Conclusions

SAOZ is a UV-visible spectrometer looking at the solar light scattered at zenith. It is a ground-based remote sensing instrument. The spectral range is 300–600 nm with a resolution of  $\sim 1$  nm. Ozone and  $\text{NO}_2$  total columns are measured by Differential Optical Absorption Spectroscopy (DOAS). The instrument is mostly sensitive during sunrise and sunset when SZA is between  $86^\circ$  and  $91^\circ$  (large optical path in the stratosphere).

SAOZ has demonstrated many advantages: completely automatic very useful in remote places and allowing measurements for all weather conditions. SAOZ is a self-calibrated instrument on wavelength using solar lines and on the constituents using laboratory absorption cross sections. Since measurements are done in the visible, it is no necessary to correct the absorption cross sections from stratospheric temperatures variations.

The application of UV-Vis NDACC Working Group recommendations in a new SAOZ retrieval called V2 was an important improvement specially after considering climatological AMF. The amplitude of seasonal variation of the difference between satellites/Dobson and SAOZ is largely reduced.

SAOZ observations are used in scientific community for different studies as shown in section 4. A continuous annual ozone dataset can be achieved with SAOZ in the polar circle allowing ozone loss estimation from the beginning of the ozone loss period that is in winter. SAOZ network with high quality measurements (error lower than 5% for  $\text{O}_3$ ) that covers all latitudes to assess the quality of long term satellite measurements as well as models validation.

The SAOZ V2 data used in this work are publicly available at NDACC database (see <http://www.ndacc.org>). The 11 French SAOZ stations are supported by IPEV (Institut Paul Emile Victor), INSU (Institut des Sciences de l'Univers) and CNES (Centre National d'Etudes Spatiales).

The author would like to thank the persons who maintain the SAOZ instruments at the different stations and her colleagues of SAOZ/CNRS team Florence Goutail, Jean-Pierre Pommereau, Manuel Nunes-Pinharanda and Eric D'Almeida. She wishes to thank Florence Goutail and Jayan Kuttippurath for Arctic and Antarctic ozone loss data, respectively. Thanks again to Florence Goutail for reviewing this chapter.

## References

1. J.P. Pommereau, F. Goutail, *Geophys. Res. Lett.*, **15**, 895 (1988)
2. A. Sarkissian, J.P. Pommereau, F. Goutail, *Geophys. Res. Lett.*, **18**, 779–782 (1991)
3. A. Sarkissian, J.P. Pommereau, F. Goutail, E. Kyrö, *Geophys. Res. Lett.*, **21**, 1319–1322 (1994)
4. U. Platt, J. Stutz, *Differential Optical Absorption Spectroscopy (DOAS), Principles and Applications* (Springer, Berlin-Heidelberg, 2008)
5. R.L. Kurucz, I. Furenlid, J. Brault, L. Testerman, *Solar flux atlas from 296 nm to 1300 nm, National Solar Observatory Atlas No. 1* (1984)

6. S. Solomon, A. L. Schmeltekopf, R. W. Sanders, *J. Geophys. Res.*, **92**, 8311–8319 (1997)
7. K. Chance, R. J. D. Spurr, *Applied Optics*, **36**, 5224–5230 (1997)
8. F. Hendrick, J.P. Pommereau, F. Goutail, R. D. Evans, D. Ionov, A. Pazmino, E. Kyrö, G. Held, P. Eriksen, V. Dorokhov, M. Gil, M. Van Roozendael, *Atmos. Chem. Phys. Discuss.*, **10**, 20405–20460 (2010)
9. K. Bogumil, J. Orphal, T. Homann, S. Voigt, P. Spietz, O.C. Fleischmann, A. Vogel, M. Hartmann, H. Bovensmann, J. Frerik, J.P. Burrows, *J. Photochem. Photobiol. A*, **157**, 167–184 (2003)
10. A.C. Vandaele, C. Fayt, F. Hendrick, C. Hermans, F. Humbled, M. Van Roozendael, M. Gil, M. Navarro, O. Puentedura, M. Yela, G. Braathen, K. Stebel, K. Tørnkvist, P. Johnston, K. Kreher, F. Goutail, A. Mieville, J.P. Pommereau, S. Khaikine, A. Richter, H. Oetjen, F. Wittrock, S. Bugarski, U. Frieß, K. Pfeilsticker, R. Sinreich, T. Wagner, G. Corlett, R. Leigh, *J. Geophys. Res.*, **110**, D08305, doi:10.1029/2004JD005423 (2005)
11. L.S. Rothman, D. Jacquemart, A. Barbe, D. Chris Benner, M. Birk, L.R. Brown, M. R. Carleer, Jr.C. Chackerian, K. Chance, L.H. Coudert, V. Dana, V.M. Devi, R.R. Gamache, A. Goldman, K.W. Jucks, A.G. Maki, S.T. Massie, J. Orphal, A. Perrin, C.P. Rinsland, M.A.H. Smith, J. Tennyson, R.N. Tolchenov, R.A. Toth, J. Vander Auwera, P. Varanasi, G. Wagner, *J. Quant. Spectrosc. Radiat. Transfer*, **96**, 139–204 (2005)
12. G. Vaughan, H.K. Roscoe, L.M. Bartlett, F. O'Connor, A. Sarkissian, M. Van Roozendael, J.C. Lambert, P.C. Simon, K. Karlsen, B.A. Kåstad Høiskar, D.J. Fish, R.L. Jones, R. Freshwater, J.P. Pommereau, F. Goutail, S.B. Andersen, D.G. Drew, P.A. Hughes, D. Moore, J. Mellqvist, E. Hegels, T. Klupfel, F. Erle, K. Pfeilsticker, U. Platt, *J. Geophys. Res.*, **102**, 1411–1422 (1997)
13. B. Mayer, A. Kylling, *Atmos. Chem. Phys.*, **5**, 1855–1877 (2005)
14. P.K. Barthia, C.G. Wellemeyer, S.L. Taylor, N. Nath, A. Gopalan, *Proceedings of the Quadrennial Ozone Symposium 2004*, (edited by C. Zerefos, Athens, 2004)
15. M. Van Roozendael, P. Peters, H.K. Roscoe, H. De Backer, A.E. Jones, L. Bartlett, G. Vaughan, F. Goutail, J.P. Pommereau, E. Kyrö, C. Wahlstrom, G. Braathen, P.C. Simon, *J. Atm. Chem.*, **29**, 55–83 (1998)
16. F. Goutail, J.P. Pommereau, C. Phillips, C. Deniel, A. Sarkissian, F. Lefevre, E. Kyrö, M. Rummukainen, P. Eriksen, S. Andersen, B.A. Kåstad Høiskar, G. Braathen, V. Dorokhov, V. Khattatov, *J. Atmos. Chem.*, **32**, 1–34 (1999)
17. F. Lefèvre, G. P. Brasseur, I. Folkins, A. K. Smith, P. Simon, *J. Geophys. Res.*, **99**, 8183–8195 (1994)
18. J. Kuttippurath, F. Goutail, J.-P. Pommereau, F. Lefèvre, H. K. Roscoe, A. Pazmiño, W. Feng, M. P. Chipperfield, S. Godin-Beekmann, *Atmos. Chem. Phys.*, **10**, 6569–6581 (2010)